Journal of Materials Chemistry C

Accepted Manuscript

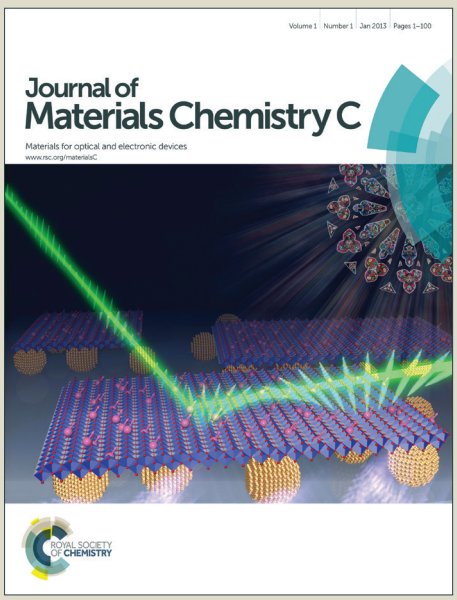

ROYAL SOCIETY OF CHEMISTRY

www.rsc.org/materialsC

Journal Name

RSCPublishing

ARTICLE

Synthesis, Structure, and Characterization of New Low-Firing Microwave Dielectric Ceramics: $(Ca_{1-3x}Bi_{2x}\Phi_x)MoO_4$

Cite this: DOI: 10.1039/x0xx00000x

Received 00th January 2012,
Accepted 00th January 2012

DOI: 10.1039/x0xx00000x

www.rsc.org/

Jing Guo[a,b], Clive A. Randall[b], Gaoqun Zhang[a], Di Zhou[a], Yuyan Chen[a], Hong Wang[a]*

A series of A-site deficient scheelite ceramics $(Ca_{1-3x}Bi_{2x}\Phi_x)MoO_4$ (x=0.005, 0.015, 0.025, 0.035, 0.05, 0.1, 0.15, 0.2, Φ: A-site vacancy) were synthesized via the solid state reaction route. The structures were analyzed using a combination of X-ray diffraction and X-ray absorption fine structure spectroscopy (Mo K-edge, Bi L_3-edge) to determine average and local structures. A series of defective scheelite $(Ca_{1-3x}Bi_{2x}\Phi_x)MoO_4$ compositions can be formed as a solid solution, and local structures of Mo and Bi indicate that MoO_4 tetrahedron and BiO_8 polyhedron become more distorted with x value. The large change in the Bi-O1 (the first shell) and Bi-O2 (the second shell) distances is an important insight into the nature of the defective structures. The statistical disorder of Bi-O bond is one order of magnitude larger than that of Mo-O bond. The microstructures and microwave dielectric properties were investigated by scanning electron microscopy and through network analyzer resonance studies. All the compositions can be sintered well below 900 °C. With slight Bi substitutions (x=0.005, 0.015), the samples exhibit improved Q×f values. At x = 0.15, temperature stable (TCF = -1.2 ppm/°C) low-firing (ST = 700 °C) microwave dielectric materials were obtained with a permittivity of 21.2 and a Q×f value of 29,300 GHz. The factors affecting dielectric properties are associated with the local structures of Mo and Bi across the solid solution.

Introduction

As wireless communication technology has increased, the demand for new microwave dielectric materials has continued[1, 2]. For low temperature co-fired ceramic (LTCC) technology, the sintering temperatures of microwave dielectric materials should be lower than the melting point of the metal electrode (silver-961 °C or copper-1042 °C). In addition, suitable dielectric constants (ε), high quality factor (Q×f) values (low dielectric losses), and small temperature coefficients of resonant frequency (TCF/$\tau_f \approx 0$ ppm/°C) are also required. The search for materials with adequate microwave dielectric properties is also a challenging problem. Thus, there is a need to develop new microwave dielectric materials and investigate the composition-structure-property relationships.[1-6]

Scheelite-type ABO_4 oxides are attractive materials due to the flexibility of substitutions, [7] which leads to great freedom in structures and properties. The ideal ABO_4 may be considered to be composed of A^{n+} cations and $(MoO_4)^{n-}$ anions. Each B-site ion is coordinated to four oxygen ions forming a BO_4 tetrahedron, and each A-site ion is surrounded by eight oxygen ions from eight different tetrahedra. As long as the overall charge is balanced, both A and B sites may accommodate ions with a range of oxidation states.[7,8] A number of ABO_4 compounds have been developed in the field of scintillation detectors, phosphors, lasers, photo-catalysts, lithium-ion batteries, and, recently, microwave dielectrics.[9-15] Among the reported scheelite ABO_4 compounds, $CaMoO_4$ has good microwave dielectric properties, with a Q×f value of 89,700 GHz and a permittivity of 10.79.[14] However, the high sintering temperature (ST = 1100 °C) and large temperature coefficient (TCF = -57 ppm/°C) limit its application. Our recent work shows that A-site substitution with the ideal stoichiometry is an effective way to tune the sintering temperature and dielectric properties of $CaMoO_4$,[16,17] also noting substitution in the structure and dielectric properties. It is known that perovskite solid solutions with good dielectric properties may exist after trivalent cations replace divalent cations at the A site.[18,19] Charge balance is maintained by the formation of A-site vacancies, an ionic compensation process. With Bi_2O_3 doping, the sintering temperature of $CaMoO_4$ may be lowered. Furthermore, it is reported that $Bi_2(MoO_4)_3$ (ε_r = 19, Q×f = 21,800 GHz)[22] has a monoclinic scheelite structure with ordered vacancies.[20,21] It may be considered as a defect scheelite in which one-third of the A ions are absent. Therefore, by Bi^{3+} replacing Ca^{2+}, it is possible to obtain a scheelite solid solution $(Ca_{1-3x}Bi_{2x}\Phi_x)MoO_4$ with low firing temperatures, and Φ is the vacant site.

Fundamental understanding on the key properties that generally control the trends from structure is enhanced through considering new structures and compositions. X-ray absorption fine structure (XAFS) spectroscopy is a powerful technique to provide quantitative information about the local structure around specific atoms. It has been widely used in many fields,

such as biology, chemistry, physics, electrons, and material science.[23-25] XAFS includes X-ray absorption near-edge structure (XANES) and extended X-ray absorption fine structure (EXAFS). XANES contains information about the geometric and electronic structure around the absorbing atom.[26] The pre-edge peak of K- or L_1- edge due to s-d transitions is sensitive to the local symmetry (octahedral and tetrahedral). The white line at the L_3-edge shows the electronic states of unfilled d orbitals. Nevertheless, the XANES theory is not fully quantitative[24], and XANES spectra are usually used as complements to the EXAFS results. Quantitative structural parameters can be obtained by the EXAFS spectra, including interatomic distances, coordination numbers, disorders in bond distances, etc.

In this work, a series of defect scheelites $(Ca_{1-3x}Bi_{2x}\Phi_x)MoO_4$ were synthesized, and their sintering behaviors, structures, microstructures, and microwave dielectric properties were all studied. The combination of XRD and XAFS provided the structural information from the point of long range scale and short range scale in the scheelite system. A systematic study of the structure-property relationship was undertaken based on the concentration of Bi/A-site vacancy.

Experimental

Polycrystalline specimens of $(Ca_{1-3x}Bi_{2x}\Phi_x)MoO_4$ (x=0.005, 0.015, 0.025, 0.035, 0.05, 0.1, 0.15, 0.2, CBM were used for abbreviations) were prepared by the solid state reaction method. Stoichiometric amounts of reagent-grade powders $CaCO_3$ (>99%, Sinopharm Chemical Reagent Co. Ltd, Shanghai, China), Bi_2O_3 (>99%, Shudu Nano-Science Co., Ltd, Chengdu, China), and MoO_3 (>99.5%, Yutong Chemical Reagents, Tianjin, China) were weighed and milled with ethanol and zirconia balls for 4 h using a planetary ball-mill. After drying, the mixtures were calcined in air at 600 ^oC for 4 h. After re-milling with zirconia balls in ethanol for 4 h, the powders with polyvinyl alcohol (PVA) binder additions were pressed into cylindrical pellets (8 mm in diameter and 4 mm in height) under a uniaxial pressure of 250 MPa. Finally, these specimens were sintered in air at 650-900 °C for 2 h.

The phase compositions and structures of densely sintered samples were determined by X-ray diffraction with Cu Kα radiation (PANalytical Empyrean) and X-ray adsorption fine structure spectroscopy. For the XRD and XAFS measurements, the sintered pellets were ground to fine powders with an agate mortar and pestle. XAFS spectra were measured at the BL14W1 beam-line of the Shanghai Synchrotron Radiation Facility (SSRF). The storage ring of SSRF was working at the energy of 3.5 GeV with a stored current of 150-210 mA. During the measurements, the beam-line was operated with a 38 pole wiggler photon source and a Si (311) double crystal monochromator. The XAFS data at the Mo K-edge and Bi L3-edge were recorded in the transmission mode at room temperature. The spectra were scanned in the range of 19800-21000 eV and 13219-14415 eV for Mo K-edge and Bi L3-edge, respectively. The data processing and fitting were performed with the use of ATHENA and ARTEMIS software.[28] Using ATHENA, all the spectra were normalized to an edge jump of 1 and the EXAFS oscillations, $\chi(k)$, were obtained by subtraction of the atomic background. For the Mo K-edge, the Fourier transformation with k^3-weight was made in the k range of ≈3-13.8Å^{-1}. For the Bi L3-edge, the Fourier transformation with k^2-weight was carried out in the k range of ≈3.3-11.2Å^{-1}. Then, the structural parameters for the starting models were put into the ARTEMIS software. The fitting was performed in the R range of ≈0.6-1.9 Å for the Mo K-edge and ≈0.8-3 Å for the Bi L3-edge. Only photoelectron single scattering was used in the data fitting.

The microstructures of sintered ceramics were observed on the fractures and surfaces using an environmental scanning electron microscope (ESEM, FEI, Quanta 200) with the low vacuum mode (80-100Pa). The bulk densities of the sintered samples were determined by the Archimedes' method. The dielectric properties at microwave frequencies were measured with a network analyzer (8720ES, Agilent, Palo Alto, CA) using the $TE_{01\delta}$ shielded cavity method. The TCF values were measured with a network analyzer and a temperature chamber (Delta 9023, Delta Design, Poway, CA), and were calculated by the following formula:

$$TCF = \frac{f_{85} - f_{25}}{f_{25}(85-25)} \times 10^6 (ppm/℃) \quad (1)$$

where f_{25} and f_{85} were the resonant frequencies at 25 ^{o}C and 85 ^{o}C, respectively.

Results and discussion

Structure Analysis by XRD and XAFS

Fig. 1(a) shows the X-ray diffraction patterns of sintered $(Ca_{1-3x}Bi_{2x}\Phi_x)MoO_4$ (x=0.005, 0.015, 0.025, 0.035, 0.05, 0.1, 0.15, 0.2) ceramics. As x increases from 0.005 to 0.15, no secondary phases can be observed, and all the peaks are successfully indexed as a tetragonal scheelite phase, which is consistent with Sleight et al. observations on $Ca_{0.88}Bi_{0.08}MoO_4$.[20] It is believed that $Ca_{0.88}Bi_{0.08}MoO_4$ (PDF# 04-008-6634) has a tetragonal scheelite structure with the space group symmetry I41/a. For x=0.2, a secondary phase comes out, which may be attributed to the changes of Bi-O bond length. (Our further study indicates that the impure phase appears at x≥0.17. The XRD patterns of CBM ceramics in the x range of 0.16-0.25 can be found in the supplementary information.) The details of Bi-O distances will be discussed in the XAFS part shown below. It is seen that the intensity of (101) peak decreases with x, which is similar to the results of scheelite materials doped with alkali and bismuth compositions $(Li_{0.5}Bi_{0.5})_xCa_{1-x}MoO_4$ and $(Na_{0.5}Bi_{0.5})_xCa_{1-x}MoO_4$.[16,17] From the literature, the A-site vacancies of $Bi_2(MoO_4)_3$ are generally considered ordered, while the vacancies of $Ca_{0.88}Bi_{0.08}MoO_4$ have no long range of ordering.[20] The A-site disordered distribution may reduce the (101) peak intensity. It is also observed that the diffraction peaks have a trend of shifting to low 2θ angles when the concentration of Bi increases. This phenomenon means that the unit cell volume may expand with increasing x. Fig. 1(b) plots the lattice parameter (a, c) and the unit cell volume (V) obtained from the XRD results. It is seen that a, c and V increase monotonically,

and a/c shows a decrease. According to the Shannon's database, the ionic radius of Bi^{3+} (1.17Å) surrounded by 8 neighbors is slightly larger than that of Ca^{2+} (1.12Å). [28] The difference between theses ionic radii may be one reason for the increase of lattice parameters. However, it is the existence of A site vacancy that makes the Mo-O tetrahedron distorted and Bi-O distances abnormal, as shown in the XAFS results below.

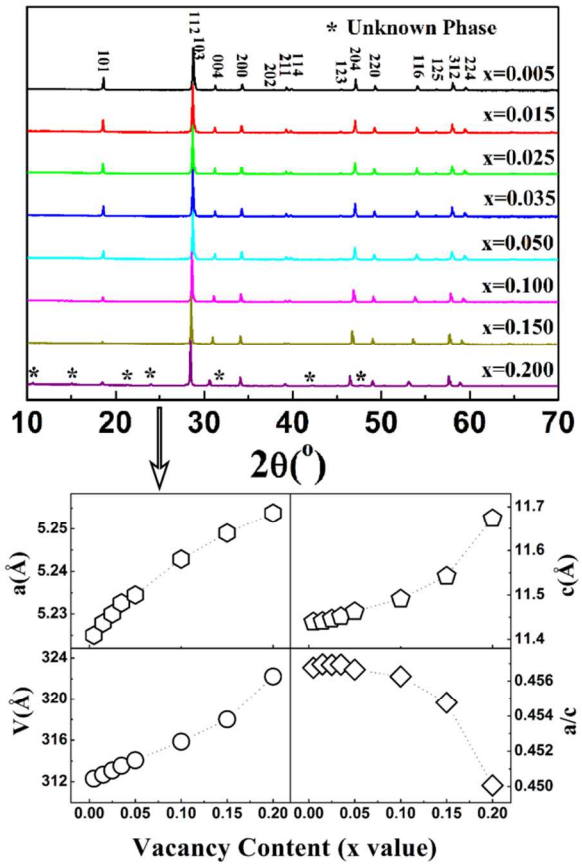

Fig. 1 X-ray diffraction patterns and cell parameters of sintered $(Ca_{1-3x}Bi_{2x}\Phi_x)MoO_4$ ceramics.

The X-ray absorption near-edge structure (XANES) spectra for selected $(Ca_{1-3x}Bi_{2x}\Phi_x)MoO_4$ compositions at the Mo K-edge are shown in Fig. 2(a). The pre-edge feature A is attributed to a 1s-4d transition, which is formally forbidden but allowed by 4d-5p hybridization[29, 30]. If the Mo cation is in a strictly octahedral environment, the pre-edge feature is forbidden. In a tetrahedral environment, the large degree of d-p orbital hybridization makes this a dominant feature. It is also reported that a very weak pre-edge peak may be observed with a distorted octahedral molybdate. From Fig. 2(a), it is seen that all the samples show a strong pre-edge feature, indicating that Mo atom in the $(Ca_{1-3x}Bi_{2x}\Phi_x)MoO_4$ ceramics is surrounded by 4 oxygen anion neighbors. With x increasing from 0.05 to 0.20, the intensity of the pre-edge peak slightly decreases, since the distortion of MoO_4 tetrahedrons may lower the extent of 4d-5p hybridization.[31, 32] It is inferred that MoO_4 tetrahedrons of $(Ca_{1-3x}Bi_{2x}\Phi_x)MoO_4$ ceramics become slightly more distorted with x increasing. Furthermore, the XANES spectra reveal that the Mo environments of all these samples are similar, and doping A site does not make great structural changes at B site.

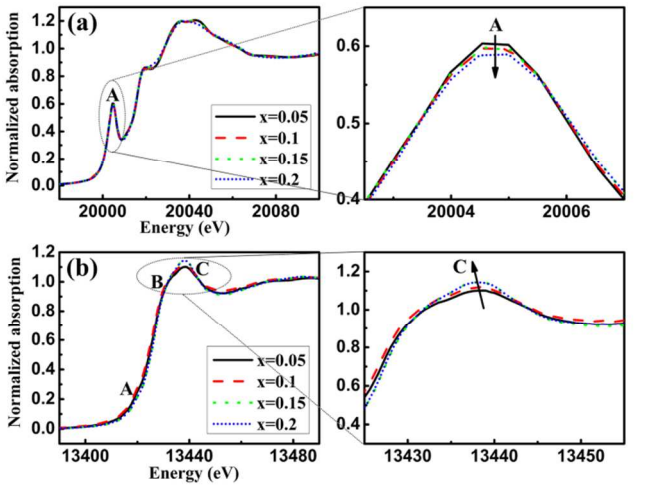

Fig. 2 Normalized XANES spectra of $(Ca_{1-3x}Bi_{2x}\Phi_x)MoO_4$ (x=0.05, 0.1, 0.15, 0.2) samples at the Mo K-edge (a) and Bi L3-edge (b).

It is known that there are 3 main features in the XANES spectra of Bi L3-edge[33-36]. The pre-edge bump A is due to a $2p^{3/2}$-6s transition. Bi 6s is considered to be filled in Bi^{3+} and empty in Bi^{5+}. Therefore, feature A is sensitive to the valence state and is usually regarded as a distinctive peak in Bi^{5+}. However, the local structure of Bi ions may also change the intensity of peak A[33]. Features B and C are attributed to a $2p^{3/2}$-6d transition and are more sensitive to the structural changes. Fig. 2(b) plots the XANES spectra of $(Ca_{1-3x}Bi_{2x}\Phi_x)MoO_4$ (x=0.05, 0.1, 0.15, 0.2) samples at the Bi L3-edge. The valence of Bi is expected to be +3, and no obvious bump in A can be observed. As x value goes up, the intensity of main peak C increases, indicating an increase in the number of unfilled d states at the Bi site. It is also seen that the position of feature C slightly shifts to the lower energies, which may reveal that the Bi-O bond length slightly rises with x, according to the inverse relation between peak locations in energy and bond length[33]. However, there are 2 types of Bi-O bonds in the Bi local environment and they may change differently. The structural details of Bi ions can be obtained from the Extended X-ray Absorption Fine Structure (EXAFS) results shown below.

Using the photoelectron single scattering theory, the EXAFS function $\chi(k)$ can be described as follows:[24, 25]

$$\chi(k) = \sum_{j=1}^{N} \chi_j(k) = \sum_{j=1}^{N} \frac{N_j S_0^2 F_j(k)}{kR_j^2} e^{-2k^2\sigma_j^2} e^{-2R_j/\lambda(k)} \sin[2kR_j + \Phi_j(k)] \quad (2)$$

$$k = [2m\,(E-E0)/\hbar^2]^{1/2} \quad (3)$$

where k is the photoelectron wave vector, E is the photon energy, E_0 is the threshold energy, the subscript j stands for type j atoms, R_j is the distance between the excited atom and neighboring atoms, N_j is the coordination number (or number of equivalent scatters), $F_j(k)$ is the backscattering amplitude, σ^2 is

the mean-square disorder of neighboring distance (Debye-Waller factor), $\lambda(k)$ is the energy-dependent XAFS mean free path, and $\Phi_j(k)$ is the phase shift. The XRD results show that our basic structural data matches Sleight et al.'s data (PDF# 04-008-6634)[20]. So these structural parameters are used for the initial impact parameters for the ARTEMIS modeling. In this model, each A-site ion is coordinated to 8 oxygen ions forming a AO_8 dodecahedron, and each B site ion is surrounded by 4 oxygen ions forming a BO_4 tetrahedron. There are three distinct Wyckoff sites in the unit cell: O 16f (x=0.1507, y=0.0086, z=0.2106), Mo 4a (x=0, y=0.25, z=0.125) and Ca/Bi 4b (x=0, y=0.25, z=0.625). The lattice parameters a and c are 5.2280 and 11.4410 Å, respectively. The Mo nearest neighbors are O1 (R_{Mo-O1}=1.781 Å), O2 (R_{Mo-O2}=2.910 Å), A1 (R_{Mo-A1}=3.697 Å, A stands for A site atom-Ca/Bi), Mo1 (R_{Mo-Mo1}=3.875 Å) and A2 (R_{Mo-A2}=3.875 Å). The Bi nearest atoms are O1 (R_{Bi-O1}=2.447 Å), O2 (R_{Bi-O2}=2.474 Å), Mo1 (R_{Bi-Mo1}=3.697 Å), O3 (R_{Bi-O3}=3.789 Å), Mo2 (R_{Bi-Mo2}=3.875 Å), and A1 (R_{Bi-A1}=3.875 Å).

Fig. 3(a) shows the extracted EXAFS oscillations $\chi(k)$ of Mo K-edge in the k space. There is little noise in the $\chi(k)$ signal, and k^3-weighted data are Fourier transformed (FT) to R space using a Hanning window in the k range of ≈3-13.8 $Å^{-1}$, as shown in Fig. 3(b). In the FT data, the peaks represent shells of neighbors around the absorbing atom. The first peak (highest) corresponds to the shortest Mo-O bond (Mo-O1). The second highest peak is mainly attributed to the Mo-A (Mo-A1, Mo-A2) and Mo-Mo (Mo-Mo1) bonds. As x value goes up, the position of the first peak is almost unchanged, suggesting that there is little change in the distance of Mo-O1. Meanwhile, its intensity decreases slightly, which reveals that the Debye-Waller factor σ^2 may change with x. For the second highest peak, there are changes in both position and intensity, implying great changes of Mo-A bonds.

The best fits of the first peak in R space are plotted in Fig. 3(c). To simplify, only the single scattering path approximation is used in the fitting procedure. In addition, the number of structural parameters used in the fits should be less than the number of independent points. For Mo K-edge, there are approximately 9 independent points in the fitting region, and 4 structural variables are chosen to refine: the distance R_{Mo-O1}, the Debye-Waller factor σ^2, the amplitude reduction factor of inelastic losses S_o^2, and the energy shift ΔE_0. From Fig. 3(c), it is seen that the fitted spectra are in good agreement with the experimental ones, which demonstrates that the first peak is mostly originated from the Mo-O1 coordination shell, and other scattering paths can be negligible. The local structural parameters obtained from the fits are listed in Table 1. The R factor is less than 2% and S_o^2 (1.049-1.080) and ΔE_0 (6.8-7.8 eV) are moderate. The shortest Mo-O distance R_{Mo-O1} is similar to that in the starting model (1.781 Å). Furthermore, the Mo-O1 distances for all the compositions are similar, which means that there are only small changes at B site. The Debye-Waller factor σ^2, representing fluctuations in interatomic distances, includes thermal and configurational (static) disorder [24]. The Debye-Waller factor of Mo-O1 bond slightly increases when x value goes up, which may indicate that the static disorder slightly rises.

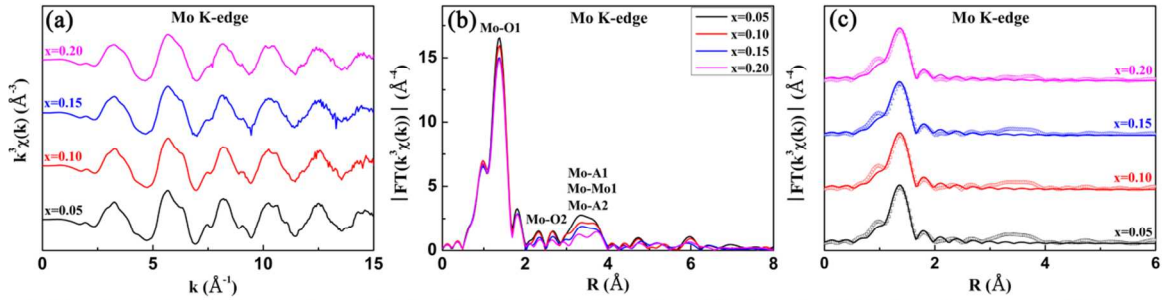

Fig. 3 k^3-weighted Mo K-edge EXAFS data (a), the magnitude of their Fourier transform (b), and the fits of the first peak (c). Circles and solid lines are experimental data and calculated results, respectively

Table 1 Structural parameters of the Mo local environment obtained by the fitting of EXAFS data. N is the coordination number, σ^2 is the Debye-Waller factor, R is the interatomic distance, R factor is the measure of the percentage misfit between the experimental and calculated data.

x	N	σ2 (Å^2)	RMo-O1 (Å)	R factor (%)
0.05	4	0.0024	1.774	0.025
0.10	4	0.0029	1.776	0.047
0.15	4	0.0033	1.775	0.043
0.20	4	0.0033	1.777	0.066

Table 2 Structural parameters of the Bi local environment obtained by the fitting of EXAFS data. N is the coordination number, σ^2 is the Debye-Waller factor, R is the interatomic distance, R factor is the measure of the percentage misfit between the experimental and calculated data.

	Bi-O1 Shell			Bi-O2 Shell			
x	N	σ^2_{Bi-O1} (Å^2)	R_{Bi-O1} (Å)	N	σ^2_{Bi-O2} (Å^2)	R_{Bi-O2} (Å)	R factor (%)
0.05	4	0.0110	2.400	4	0.0123	2.624	3.52
0.10	4	0.0117	2.343	4	0.0109	2.548	4.87
0.15	4	0.0208	1.984	4	0.0330	2.703	1.51
0.20	4	0.0162	1.937	4	0.0233	2.712	1.05

Fig. 4(a) shows the extracted EXAFS oscillations $\chi(k)$ of Bi L3-edge in the k space. Compared with Mo K-edge data, there are more noises in the $\chi(k)$ signal at Bi L3-edge, especially in the high k region. Therefore, the Fourier transformations with k^2-weight are carried out using a Hanning window in the k range of ≈3.3-11.2Å^{-1}, as shown in Fig. 3(b). It is seen that there are three major peaks. The first and second peaks correspond to Bi-O1 and Bi-O2 bonds, respectively. The main contributions of the third peak come from Bi-Mo (Bi-Mo1, Bi-Mo2) and Bi-A (Bi-A1) bonds. As x value goes up, the first peak shifts to a lower R value, and the second peak shifts to a higher R value. This phenomenon reveals that the Bi nearest O atoms (O1, O2) behave differently when the concentration of Bi increases: The Bi-O1 distance may increase, while the Bi-O2 distance may decrease.

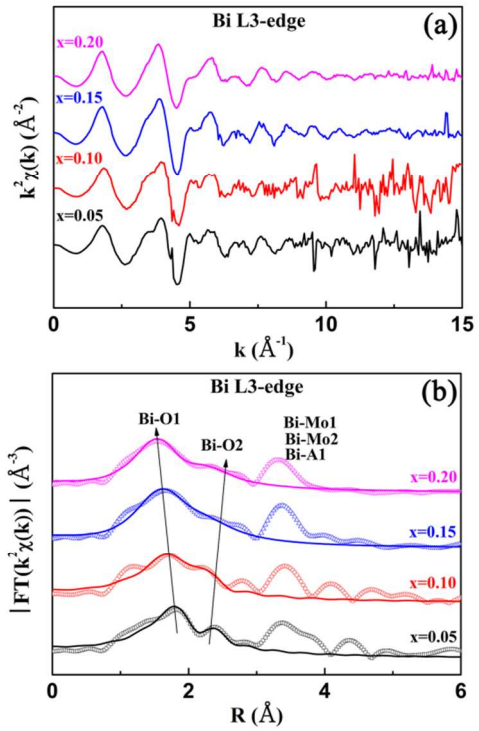

Fig. 4 k^2-weighted Bi L3-edge EXAFS data (a), the magnitude of their Fourier transform and the fits of the first and second peaks (b). Circles and solid lines are experimental data and calculated results, respectively.

The best fits of the first and second peaks in R space are plotted in Fig. 4(b). In the fitting procedure, there are approximately 10 independent points in the fitting region and 6 structural parameters are allowed to vary: the distances (R_{Bi-O1}, R_{Bi-O2}), the Debye-Waller factors (σ^2_{Bi-O1}, σ^2_{Bi-O2}), the amplitude reduction factor of inelastic losses S_o^2, and the energy shift ΔE_0. In order to minimize the number of structural variables, S_o^2 and ΔE_0 for Bi-O1 and Bi-O2 scattering paths are constrained to be the same. The fitted spectra match well with the experimental ones, indicating that the first two peaks are mainly attributed to the Bi-O coordination shells (Bi-O1, Bi-O2), justifying our initial approximation. Table 2 lists the local structural parameters obtained from the fits. The R factor, S_o^2 (1.064-0.418) and ΔE_0 (0.8-18.9 eV) are acceptable. Compared with the interatomic distances in the starting model (R_{Bi-O1}=2.447 Å, R_{Bi-O2}=2.474 Å), the differences between the Bi-O1 bond length and Bi-O2 bond length become increasingly larger. The Bi-O1 distance shows a decrease, while the Bi-O2 distance shows an increase. These results reveal that the Bi-O polyhedron becomes distorted when x rises. In order to observe the structural changes clearly, Fig. 5 plots a schematic illustration of the A-site local environment. After Bi^{3+} replaces the Ca^{2+}, the A-site vacancy appears, and this in turn has a great effect on the local structure. As the concentration of vacancies increases, the Bi-O polyhedron gets more and more distorted. It is known that $Bi_2(MoO_4)_3$ can be viewed as a defective scheelite structure with space group $P2_1/c$ (Monoclinic, a=7.685 Å, b=11.491 Å, c=11.929 Å, β=115.4°). Bi ion has 8 oxygen neighbors, and the Bi-O bonds can be divided into 2 distinct groups: R_{Bi-O1}=2.12-2.35 Å, and R_{Bi-O2}=2.60-2.93 Å.[21] Therefore, when x value is large, the monoclinic scheelite phase may come out, as shown in the supplementary information. From Table 2, it is observed that the shortest Bi-O distance (Bi-O1) of $(Ca_{0.55}Bi_{0.3}\Phi_{0.15})MoO_4$ and $(Ca_{0.4}Bi_{0.4}\Phi_{0.2})MoO_4$ is smaller than that of $Bi_2(MoO_4)_3$, which may result from the disordered distribution of vacancies. The changes of Bi-O distances are supposed to be the main factors reflected in the XRD data. It is also seen that the Debye-Waller

factor of Bi-O bond is one order of magnitude larger than that of Mo-O bond. A higher Debye-Waller factor may indicate a higher statistical disorder. In the assumed structural model, Bi locates at the center of oxygen dodecahedron. However, the Bi may move off-center in the oxygen polyhedron. The fluctuation of Bi-O distances makes the Debye-Waller factor large, somewhat similar to the order-disorder in the Bi-pyrochlore systems.[37]

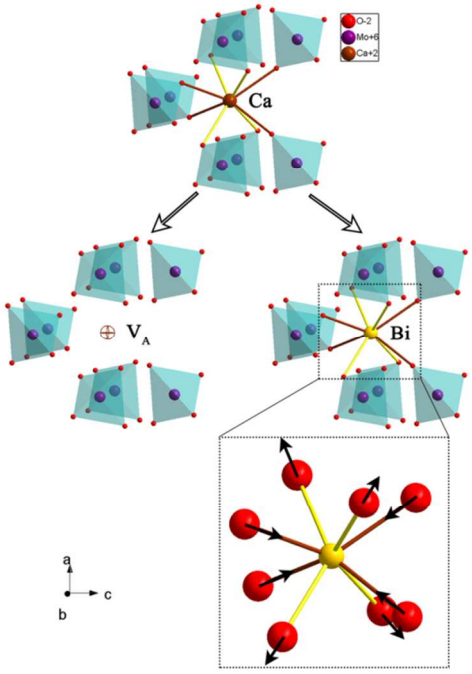

Fig. 5 Schematic illustration of local structures at A site. (V_A, Vacancy at A site; Brown bond, Bi-O1 bond; Yellow bond, Bi-O2 bond)

Characterization

Fig. 6 presents the SEM images of fractures and surfaces (Inserts) of $(Ca_{1-3x}Bi_{2x}\Phi_x)MoO_4$ ceramics with low amounts of Bi and high amounts of Bi. The grain size of $(Ca_{0.985}Bi_{0.01}\Phi_{0.005})MoO_4$ and $(Ca_{0.925}Bi_{0.05}\Phi_{0.025})MoO_4$ lies in the range of 1-6 μm, which is smaller than that of the ceramics with x=0.1 and x=0.2 (2-11 μm). With the Bi substitution, the growth is faster, and the sinterability is also improved at low firing temperatures. It is also seen that the samples with high amounts of Bi have more pores with round shapes, which may result from the volatilization of Bi_2O_3. It is noted that the $(Ca_{0.4}Bi_{0.4}\Phi_{0.2})MoO_4$ has the largest ratio of pores, which may reduce its density.

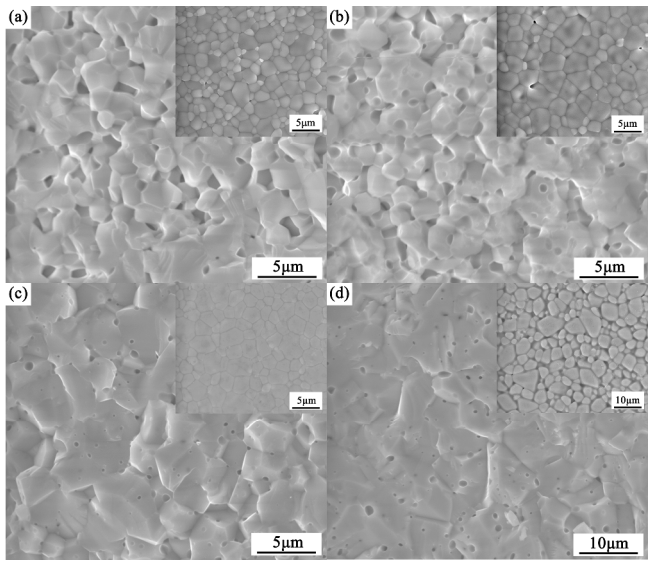

Fig. 6 SEM images for (a) CBM-0.005 ceramic sintered at 900 °C for 2 h, (b) CBM-0.025 ceramic sintered at 800 °C for 2 h, (c) CBM-0.1 ceramic sintered at 700 °C for 2 h, and (d) CBM-0.2 ceramic sintered at 700 °C for 2 h.

The sintering temperatures and densities of $(Ca_{1-3x}Bi_{2x}\Phi_x)MoO_4$ ceramics as a function of x value are shown in Fig. 7. It is well known that Bi_2O_3 is an oxide with a low melting point. Therefore, with x increasing from 0.005 to 0.2, the sintering temperature reduces from 900 °C to 700 °C. Glass-free low-firing microwave dielectric materials $(Ca_{1-3x}Bi_{2x}\Phi_x)MoO_4$ can be obtained, which is consistent with the hypothesis in the introduction. In the x range of 0.005-0.15, the relative densities of $(Ca_{1-3x}Bi_{2x}\Phi_x)MoO_4$ ceramics are over 90 %, indicating that all the specimens are well sintered and densified. As x=0.2, the sample shows a low relative density of below 90%. Combined with SEM results, this phenomenon may arise from the volatilization of Bi_2O_3.

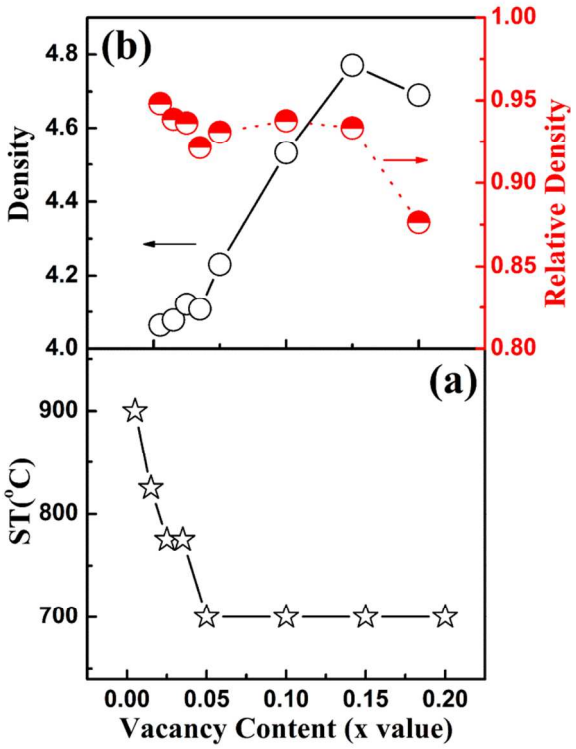

Fig. 7 Sintering temperatures (a) and densities (b) of $(Ca_{1-3x}Bi_{2x}\Phi_x)MoO_4$ ceramics as a function of x value.

Fig. 8(a) plots the microwave permittivities of $(Ca_{1-3x}Bi_{2x}\Phi_x)MoO_4$ ceramics sintered at their optimal temperatures. With x going up, the measured permittivities increase step by step. Clausius-Mosotti equation is a popular model to predict the permittivities of materials. In this work, C-M equation is used to calculate the relative permittivities of $(Ca_{1-3x}Bi_{2x}\Phi_x)MoO_4$ samples:

$$\varepsilon=\frac{3V_m+8\pi\alpha_D}{3V_m-4\pi\alpha_D} \quad (4)$$

where V_m represents the molar volume; α_D represents the molecular polarizability. The ion additivity rule is used to derive the molecular polarizability of $(Ca_{1-3x}Bi_{2x}\Phi_x)MoO_4$ samples:[38]

$$\alpha_D(CBM)=(1-3x)\alpha_D(Ca^{2+})+2x\alpha_D(Bi^{3+})+\alpha_D(Mo^{6+})+4\alpha_D(O^{2-}) \quad (5)$$

The ion polarizabilities of Bi^{3+}, Ca^{2+}, Mo^{6+}, and O^{2-} are 6.12, 3.16, 3.28, and 2.01 $Å^3$, respectively.[14,38] After Bi^{3+} ions replace Ca^{2+} ions, the molecular polarizability (α_D=14.48+2.76x), as well as the molar volume (V_m), increases. Consequently, the calculated permittivities remain almost unchanged, as shown in Figure 8(a). For the samples with small x values (0.005-0.05), the measured permittivities match well with the calculated ones. For the samples with large x values (0.1-0.2), there are large deviations between the measured and calculated permittivities. The large deviations may be attributed to the structural changes discussed in the XAFS part. For the ideal tetragonal scheelite $CaMoO_4$, A-site ions have two types of adjacent oxygen ions, and the difference between these two bond lengths is small (0.01-0.025 Å).[39-41] It is reported that the measured dielectric constant of $CaMoO_4$ is in a good agreement with the calculated one (Deviation=3.1%).[14] After the trivalent cation Bi^{3+} substitutes for the divalent cation Ca^{2+}, the AO_8 polyhedron may adjust its configuration to adapt to the vacancy and the large cation. In the present work, Bi-O1 distance and Bi-O2 distance change oppositely, and the difference becomes larger and larger. At x=0.2, Bi-O2 distance is even 0.775 Å larger than that of Bi-O1. These large structural adjustments may make A-site ion polarizabilities increase. In addition, the ion polarizability of Mo^{6+} may also slightly increase with x increasing because of the distortion of MoO_4 tetrahedron. As a result, for $(Ca_{1-3x}Bi_{2x}\Phi_x)MoO_4$ ceramics with high amounts of Bi, the measured permittivities are larger than that of calculated by C-M equation. Considering the structural similarity, it may be predicted that the dielectric constants of Bi-doping scheelites $(A'_{1-3x}A''_{2x}\Phi_x)BO_4$ (A'=Ca, Sr, Ba , A''=Bi, B=Mo, W) will be larger than that of pure ceramics.

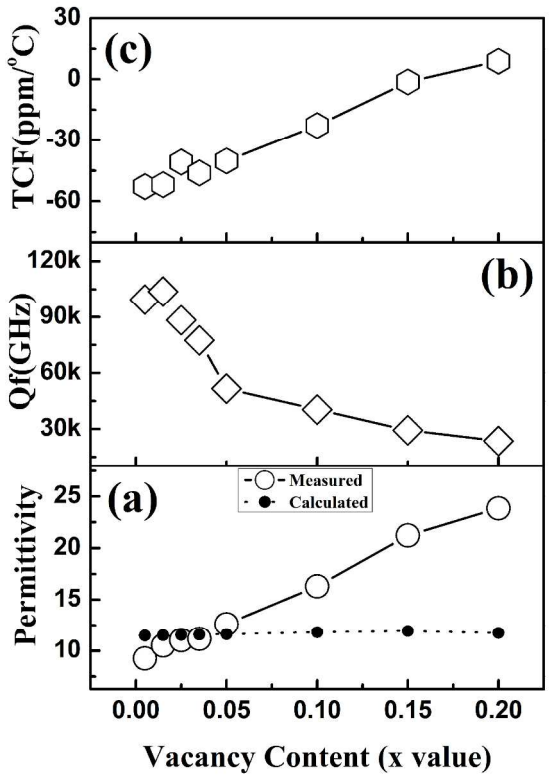

Fig. 8 Permittivies (a), Q×f values (b) and TCF values (c) of $(Ca_{1-3x}Bi_{2x}\Phi_x)MoO_4$ ceramics as a function of x value.

The curve of Q×f values versus the x value is shown in Fig. 8(b). It is observed that the dielectric losses at the microwave frequency are sensitive to the Bi^{3+} substitution and the A-site vacancy. As x value goes up, the Q×f value of $(Ca_{1-3x}Bi_{2x}\Phi_x)MoO_4$ first slightly increases from 99,410 GHz to

103,750 GHz and then dramatically decreases to 23,540 GHz. For the samples with x=0.005-0.025, there are only small variations in the Q×f values. $(Ca_{0.085}Bi_{0.01}\Phi_{0.005})MoO_4$ and $(Ca_{0.955}Bi_{0.03}\Phi_{0.015})MoO_4$ exhibit even better dielectric properties than $CaMoO_4$ (Q×f = 89,700 GHz). At x=0.025, the Q×f value starts to deteriorate. It is well known that the dielectric losses can be influenced by a number of intrinsic and extrinsic factors[42-44]. Intrinsic losses are associated with the crystal structure, frequency, and temperature. Extrinsic losses arise from imperfections in the crystals, including impurities, pores, vacancies, microstructural defects, size and shapes of grains, site orders, etc. For the A-site deficient scheelites $(Ca_{1-3x}Bi_{2x}\Phi_x)MoO_4$ case, the porosity, grain, structure, and order-disorder may be the main factors controlling the Q×f values. The existence of pores originated from the volatilization of Bi_2O_3 may decrease the Q×f values. However, for the samples with a low Bi-doping, especially $x \leq 0.05$, the contributions of pores can be ignored. The ceramics with small percentages of deficiencies/nonstoichiometry may have an enhanced sinterability[45]. The sinterability may be one reason for the improvement of Q×f values with a very low Bi-doping. The structure of $(Ca_{1-3x}Bi_{2x}\Phi_x)MoO_4$, to some extent, is related to the A-site order. The disordered distribution of vacancies may distort the MoO_4 tetrahedron and BiO_8 polyhedron observed in the XAFS spectra. With x increasing, the disordered vacancies increase, and the polyhedron become more distorted, which may make the Q×f values deteriorate. (We will discuss the disorders from the point of vibrational spectra in the further study.) However, the $(Ca_{1-3x}Bi_{2x}\Phi_x)MoO_4$ ceramic with a near-zero TCF value (TCf = -1.2 ppm/^{o}C) exhibits a good Q×f value (29,300 GHz), as shown in Fig. 5. It is also seen that the TCf values can be tuned from -52.8 to +8.9 ppm/^{o}C with the Bi substitution.

Conclusions

New glass-free low firing materials $(Ca_{1-3x}Bi_{2x}\Phi_x)MoO_4$ with good microwave dielectric properties were introduced in this study. All the compositions can be sintered well below 900 ^{o}C. The XRD patterns reveal that $(Ca_{1-3x}Bi_{2x}\Phi_x)MoO_4$ ($0.005 \leq x \leq 0.2$) are defect scheelite solid solutions with a tetragonal structure. No secondary phase can be observed in the x range of 0.005-0.15. The local structure of Mo obtained from XAFS results demonstrates that the MoO_4 tetrahedron becomes slightly distorted, and the static disorder increases with x. The distortion of BiO_8 polyhedron also can be observed from the local structure of Bi. Especially, there are severe distortions for the samples with a high amount of Bi. When x value goes up, the Bi-O1 and Bi-O2 distances show a decrease and increase, respectively. The statistical disorder of the Bi-O bond is one order of magnitude larger than that of the Mo-O bond. As x value increases from 0.005 to 0.2, the permittivity increases from 9.3 to 23.9, the Q×f value first increases from 99,400 to 103,800 GHz and then decreases to 23,500 GHz, and the TCF values shift from -52.8 to +8.9 ppm/^{o}C. $(Ca_{0.985}Bi_{0.01}\Phi_{0.005})MoO_4$ and $(Ca_{0.955}Bi_{0.03}\Phi_{0.015})MoO_4$ exhibit improved Q×f values (99,400 GHz and 103,800 GHz), and $(Ca_{0.55}Bi_{0.3}\Phi_{0.15})MoO_4$ exhibits excellent overall dielectric properties with ST=700 ^{o}C, ε_r = 21.2, Q×f = 29,300 GHz, and TCF = -1.2 ppm/^{o}C. The distortion of AO_8 polyhedron is considered to be the main factor increasing the measured permittivities and making deviations between the measured permittivities and calculated ones. The deterioration of Q×f values may be attributed to the A-site disorder and distortions of AO_8 and BO_4 polyhedrons. With a high Bi-doping, pores originating from the volatilization of Bi_2O_3 may also decrease the Q×f values.

Acknowledgements

This work was supported by National Science Foundation of China (61025002, 51202182), the Center for Dielectric Studies industrial membership fund, and the SRFDP-RGC Joint Research Project 2013/14 (20130201140002). The authors would like to thank the administrators in the BL14W1 beam lines of Shanghai Synchrotron Radiation Facility (SSRF) for their help in the XAFS measurements. The authors gratefully acknowledge technical assistance from Amanda Baker (Basics), Gino Tambourine (XRD), and Julie Anderson (SEM) at The Pennsylvania State University (Penn State). The authors also thank Joanne Aller for her help in the preparation of this manuscript. Jing Guo also wishes to thank China Scholarship Council (CSC) for providing the opportunity to study as a visiting scientist at Penn State.

Notes and references

[a] Electronic Materials Research Laboratory, Key Laboratory of the Ministry of Education & International Center for Dielectric Research, Xi'an Jiaotong University, Xi'an, 710049, China.

[b] Center for Dielectrics and Piezoelectrics, Materials Research Institute, The Pennsylvania State University, University Park, PA 16802, USA.

Electronic Supplementary Information (ESI) available: [X-ray diffraction patterns of CBM ceramics in the x range of 0.16-0.25].

1 R. J. Cava, *J. Mater. Chem.*, 2001, **11**, 54-62.
2 I. M. Reaney and D. Iddles, *J. Am. Ceram. Soc.*, 2006, **89**, 2063-2072.
3 M. T. Sebastian and H. Jantunen, *Int. Mater. Rev.*, 2008, **53**, 57-90.
4 W. Wersing, *Curr. Opin. Solid State Mat. Sci.*, 1996, **1**, 715-731.
5 T. A. Vanderah, *Science*, 2002, **298**, 1182-1184.
6 M. Valant and D. Suvorov, *J. Eur. Ceram. Soc.*, 2004, **24**, 1715-1719.
7 A. W. Sleight and W. J. Linn, *Ann.NY Acad.Sci.*, 1976, **272**, 22-44.
8 A. T. Aldred, *ACS Symp. Ser.*, 1984, **246**, 305-314.
9 V. B. Mikhailik, H. Kraus, G. Miller, M. S. Mykhaylyk and D. Wahl, *J. Appl. Phys.*, 2005, **97**, 083523.
10 N. Faure, C. Borel, M. Couchaud, G. Basset, R. Templier and C. Wyon, *Appl. Phys. B-Lasers Opt.*, 1996, **63**, 593-598.
11 L. S. Cavalcante, V. M. Longo, J. C. Sczancoski, M. A. P. Almeida, A. A. Batista, J. A. Varela, Mo. O. Orlandi, E. Longo and M. S. Liu, *CrystEngComm*, 2012, **14**, 853-868.
12 W. F. Yao and J. H. Ye, *J. Phys. Chem. B*, 2006, **110**, 11188-11195.
13 N. Sharma, K. M. Shaju, G. V. S. Rao, B. V. R. Chowdari, Z. L. Dong and T. J. White, *Chem. Mater.,* 2004, **16**, 504-512.
14 G. K. Choi, J. R. Kim, S. H. Yoon and K. S. Hong, *J. Eur. Ceram. Soc.,* 2007, **27**, 3063-3067.
15 S. H. Yoon, D. W. Kim, S. Y. Cho and K. S. Hong, *J. Eur. Ceram. Soc.,* 2006, **26,** 2051-2054.

16 D. Zhou, H. Wang, Q. P. Wang, X. G. Wu, J. Guo, G. Q. Zhang, L. Shui, X. Yao, C. A. Randall, L. X. Pang, and H. C. Liu, *Funct. Mater. Lett.*, 2010, **3**, 253-257.
17 J. Guo, D. Zhou, Y. Li, T. Shao, Z. M. Qi, B. B. Jin, and H. Wang, Structure-Property Relationships of Novel Microwave Dielectric ceramics with Low Sintering Temperatures: $(Na_{0.5}Bi_{0.5})_xCa_{1-x}MoO_4$, Submitted.
18 R. Ubic, G. Subodh, M. T. Sebastian, D. Gout and T. Proffen, *Chem. Mater.*, 2008, **20**, 3127-3133.
19 I. S. Kim, W. H. Jung, Y. Inaguma, T. Nakamura and M. Itoh, *Mater. Res. Bull.*, 1995, **30**, 307-316.
20 A. W. Sleight, K. Aykan and D. B. Rogers, *J. Solid State Chem.*, 1975, **13**, 231-236.
21 Vandenel.Af and G. D. Rieck, *Acta Crystallogr. Sect. B*, 1973, **29**, 2433-2436.
22 D. Zhou, H. Wang, L. X. Pang, C. A. Randall and X. Yao, *J. Am. Ceram. Soc.*, 2009, **92**, 2242-2246.
23 J. J. Rehr, J. M. Deleon, S. I. Zabinsky and R. C. Albers, *J. Am. Chem. Soc.*, 1991, **113**, 5135-5140.
24 J. J. Rehr and R. C. Albers, *Rev. Mod. Phys.*, 2000, **72**, 621-654.
25 P. A. Lee, P. H. Citrin, P. Eisenberger and B. M. Kincaid, *Rev. Mod. Phys.*, 1981, **53**, 769-806.
26 H. Asakura, T. Shishido, S. Yamazoe, K. Teramura and T. Tanaka, *J. Phys. Chem. C*, 2011, **115**, 23653-23663.
27 B. Ravel and M. Newville, *J. Synchrot. Radiat.*, 2005, **12**, 537-541.
28 R. D. Shannon, *Acta Crystallogr. Sect. A*, 1976, **32**, 751-767.
29 F. W. Kutzler, C. R. Natoli, D. K. Misemer, S. Doniach and K. O. Hodgson, *J. Chem. Phys.*, 1980, **73**, 3274-3287.
30 R. Radhakrishnan, C. Reed, S. T. Oyama, M. Seman, J. N. Kondo, K. Domen, Y. Ohminami and K. Asakura, *J. Phys. Chem. B*, 2001, **105**, 8519-8530.
31 N. F. D. Verbruggen, G. Mestl, L. M. J. Vonhippel, B. Lengeler and H. Knozinger, *Langmuir*, 1994, **10**, 3063-3072.
32 Z. Zhai, A. Getsoian and A. T. Bell, *J. Catal.*, 2013, **308**, 25-36.
33 N. Jiang and J. C. H. Spence, *J. Phys.-Condes. Matter*, 2006, **18**, 8029-8036.
34 A. Q. Pham, F. Studer, N. Merrien, A. Maignan, C. Michel and B. Raveau, *Phys. Rev. B*, 1993, **48**, 1249-1253.
35 S. Salemsugui, E. E. Alp, S. M. Mini, M. Ramanathan, J. C. Campuzano, G. Jennings, M. Faiz, S. Pei, B. Dabrowski, Y. Zheng, D. R. Richards and D. G. Hinks, *Phys. Rev. B*, 1991, **43**, 5511-5515.
36 S. M. Heald, D. Dimarzio, M. Croft, M. S. Hegde, S. Li and M. Greenblatt, *Phys. Rev. B*, 1989, **40**, 8828-8833.
37 I. Levin, T. G. Amos, J. C. Nino, T. A. Vanderah, I. M. Reaney, C. A. Randall and M. T. Lanagan, *J. Mater. Res.*, 2002, **17**, 1406-1411.
38 R. D. Shannon, *J. Appl. Phys.*, 1993, **73**, 348-366.
39 E. Gurmen, E. Daniels, and J. S. King, *J. Chem. Phys.*, 1971, **55**, 1093-1097.
40 S. N. Achary, S. J. Patwe, M. D. Mathews and A. K. Tyagi, *J. Phys. Chem. Solids*, 2006, **67**, 774-781.
41 R. M. Hazen, L. W. Finger and J. W. E. Mariathasan, *J. Phys. Chem. Solids*, 1985, **46**, 253-263.
42 V. L. Gurevich and A. K. Tagantsev, *Adv. Phys.*, 1991, **40**, 719-767.
43 H. Tamura, *J. Eur. Ceram. Soc.*, 2006, **26**, 1775-1780.
44 S. J. Penn, N. M. Alford, A. Templeton, X. R. Wang, M. S. Xu, M. Reece, and K. Schrapel, *J. Am. Ceram. Soc.*, 1997, **80**, 1885-1888.
45 K. P. Surendran, M. T. Sebastian, P. Mohanan, R. L. Moreira and A. Dias, *Chem. Mater.*, 2005, **17**, 142-151.

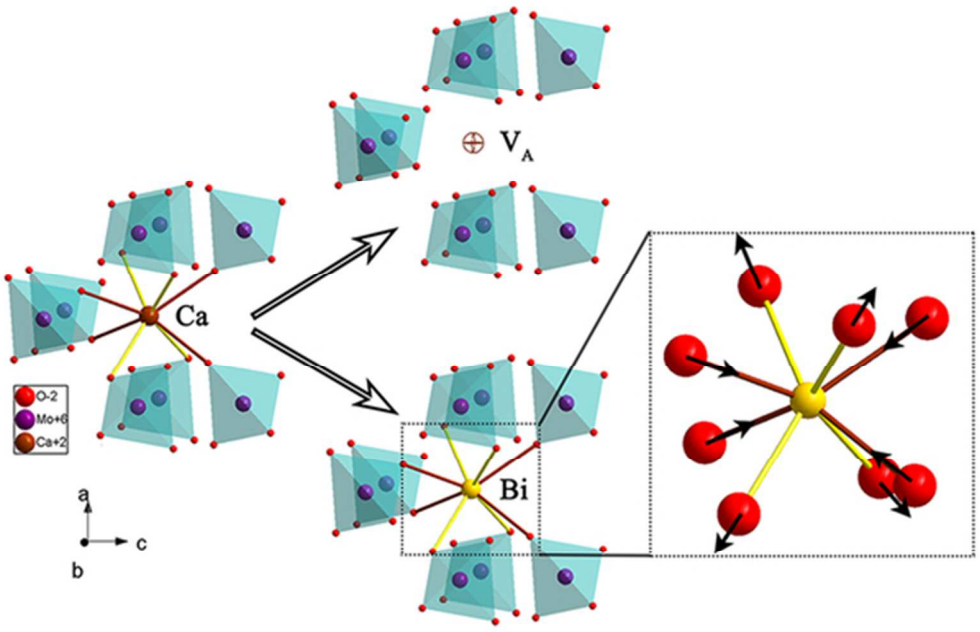

51x33mm (300 x 300 DPI)